Article type: Original Article

Robotic Gripper with Multimodal Tactile Sensor Using Triboelectric–Magnetoelastic Hybrid Mechanism for Intelligent Fruits Sorting

Chenhao Zhang[1,2], Liang Xu[3], Xiao Lu[1], Mingxuan Fan[1], Xiaofei Bu[1,2], Yingzhong Tian[1], Long Li[1], Tao Jin[1*], Yangqiao Lin[1,2*], and Chengkuo Lee[4,5*]

[1] Shanghai Key Laboratory of Intelligent Manufacturing and Robotics, School of Mechatronic Engineering and Automation, Shanghai University, Shanghai 200444, China.

[2] National Key Laboratory of Aerospace Mechanism, Shanghai 201108, China.

[3] Shanghai Xiaoyuan Innovation Center, Shanghai 200237, China.

[4] Department of Electrical and Computer Engineering, National University of Singapore, 4 Engineering Drive 3, Singapore 117576, Singapore.

[5] Center for Sensors and MEMS, National University of Singapore, 4 Engineering Drive 3, Singapore 117576, Singapore.

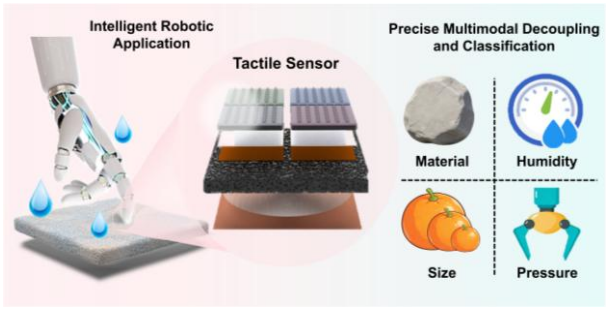
Chenhao Zhang, Liang Xu and Xiao Lu have contributed equally to this work.

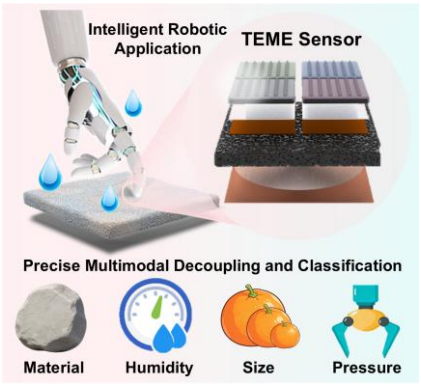
*Corresponding author. Tao Jin, robjin@shu.edu.cn; Yangqiao Lin, linyangqiao@shu.edu.cn; Chengkuo Lee, elelc@nus.edu.sg.

Highlights

- A self-powered triboelectric-magnetoelastic tactile sensor is developed by integrating a microstructured triboelectric array with an environmentally stable microporous magnetoelastic layer.
- The magnetoelastic channel provides an independent mechanical dimension to suppress force-induced interference, enabling a recognition accuracy of 99.17% across 60 coupled material–humidity–force states and outperforming the triboelectric sensor alone.
- Integrated with a robotic gripper, the sensor system achieves 98.75% recognition accuracy for fruit-humidity classes and enables intelligent fruit sorting application under controlled variable-humidity conditions.

TOC





Abstract

Flexible tactile sensor is a core technology for intelligent robots in environmental interaction and cognitive decision-making. The existing multimodal sensing approaches generally have problems such as coupled sensing attributes, severe force interference, and poor environmental robustness. This paper reports a flexible tactile sensor based on triboelectric-magnetoelastic hybrid mechanism to decouple multimodal information for intelligent fruits sorting. The sensor integrates the triboelectric and magnetoelastic effects to achieve self-powered sensing. An arrayed triboelectric sensing layer with microstructures offers the sensitivity to multiple stimuli while a microporous magnetoelastic sensing layer is utilized to provide stable mechanical information with strong anti-interference ability. By combining with deep learning algorithms, the robotic gripper with this sensor precisely decouples multidimensional tactile information including material, contact force, humidity, and object size. Crucially, integrating the magnetoelastic module enables a remarkable comprehensive recognition accuracy of 99.17%

across 60 hybrid attribute groups under laboratory conditions, substantially outperforming the standalone triboelectric module. Furthermore, it delivers a 98.75% recognition accuracy across 8 hybrid attribute classes during the intelligent fruit picking scenario. This signal fusion outperforms single mechanisms and reveals deep-level information, offering a valuable path toward acquiring high-dimensional tactile information for intelligent robots.

Keywords Triboelectric sensors; Magnetoelastic sensors; Multimodal decoupling; Machine learning; Intelligent fruits sorting

1 Introduction

Currently, intelligent robots frequently utilize visuo-tactile integration to perceive external stimuli[1]. Although visual systems can provide crucial spatial information[2], tactile approaches generally exhibit distinct advantages during the perception involving highly detailed characteristics such as surface roughness and material composition[3-5]. Recent advances in flexible sensors based on diverse sensing mechanisms and structural designs have further expanded their applications in wearable monitoring, motion sensing, human–machine interaction, and intelligent robotics [6-12]. Versatile tactile sensors endow robots with the direct capability to perceive external physical stimuli, laying a critical perceptual foundation for robust decision-making in complex, unstructured scenarios[13-17]. From enabling soft robots to perform adaptive grasping[15] to allowing biomimetic robots to execute thermal gradient tracking and hazard avoidance[16], tactile sensing fundamentally expands the cognitive boundaries of robotic manipulation. However, tactile perception during dynamic robotic grasping operations always involves multidimensional physical information, and multiple physical attributes such as material type, size, softness, and ambient relative humidity (RH), are intrinsically coupled together[18-25]. Conventional sensing methods are typically designed to sense individual properties, e.g., utilizing the thermoelectric effect for temperature[26-27], the piezoelectric effect for stiffness[28-29], the piezoresistive effect for roughness[30-31], or optical fiber sensing for curvature[32-33]. Note that contact force is a highly critical factor for handling fragile objects in autonomous operations, whereas it may induce severe signal interference and superimpose cross-coupling effects onto the sensing of other object properties[23, 34-36]. For instance, tactile sensors based on the metallic thermoresistive effect[20] suffer from contact force-induced interference during temperature measurement, because the embedded metal wires undergo significant tensile and bending deformations under contact pressure, which directly leads to severe distortion of the electrical output signal. In the context of smart farming, robotic gripper with effective tactile sensor represents a crucial development direction for agricultural robots[37], where advanced tactile sensors can facilitate precise sorting and management by identifying fruit attributes[15]. However, during the actual harvesting process, sensors are inevitably subjected to simultaneous interferences from complex external environmental factors[38], such as environmental moisture caused by unpredictable weather, as well as dynamic picking forces. Consequently, this necessitates a sophisticated integration strategy to explicitly eliminate mutual interference and achieve precise

attribute decoupling, thereby enhancing the generalization capability of individual sensors in real-time fruit harvesting scenarios.

Triboelectric nanogenerator (TENG)-based sensing technology offers a highly promising pathway for multimodal sensing. Rooted in contact electrification and electrostatic induction, TENGs possess the intrinsic capability to distinguish target object properties based on triboelectric polarity differences and surface microstructures[39-42]. Moreover, owing to the influence of adsorbed water molecules on surface-charge retention and interfacial contact electrification, TENGs are inherently sensitive to ambient humidity, enabling humidity-related changes at the contact interface to be reflected in their electrical outputs.[43]. Notably, featuring intrinsic merits such as excellent flexibility, compact structure, and outstanding scalability, TENGs can be readily integrated with diverse sensing mechanisms to expand the detectable factors of object attributes[44-48]. Although researchers have leveraged these formidable integration advantages to develop diverse TENG-based hybrid sensing systems incorporating piezoelectric[49], piezoresistive[50], or capacitive[3] mechanisms, these integrated devices remain universally susceptible to contact force interference when sensing other physical modalities. This force-induced signal drift severely degrades the accuracy of target recognition. For instance, in triboelectric sensing systems aimed at material identification, the electrical output amplitude is governed not only by the intrinsic electron affinity of the target material but also by the micro-scale effective contact area[35]. Consequently, varying grasping pressures can drastically alter the signal, making it challenging to distinguish whether a signal fluctuation originates from a change in the target material or merely a dynamic shift in the applied force. Therefore, introducing an independent, highly robust force-sensing strategy is imperative to explicitly resolve these cross-coupling bottlenecks and unlock accurate multidimensional tactile perception.

The magnetoelastic effect is a method that uses mechanical stress to change the spacing of micromagnets and the arrangement of dipoles in flexible composites to generate a changing magnetic field[51]. When combined with metal coils, mechanical energy can be converted into electrical energy through Faraday's principle of electromagnetic induction[52-53], thus becoming a self-powered magnetoelastic generator (MEG). As a new energy conversion approach, MEG is not only minimally affected by external interference factors, but also has flexible and highly sensitive force perception capabilities[51, 54-56]. Owing to these features, MEG and TENG exhibit excellent compatibility and complementarity, enabling their seamless integration. The high force sensitivity of MEG can not only accurately record the magnitude of

contact force during tactile perception, but also compensate for the inherent drawback of TENG sensing that it is susceptible to external force interference. Meanwhile, the triboelectric array makes up for the limitation of MEG in limited recognizable modalities. In addition, deep learning algorithms are widely used for detailed feature extraction and classification of sensing signals[41, 57]. For instance, deep neural networks have been successfully employed to fuse multimodal signals from a hybrid triboelectric and capacitive sensor, achieving an outstanding recognition accuracy of 98.46% across twelve different object samples[3]. Hence, a tailored algorithm can fully exploit the complementary advantages of the multimodal sensor based on both triboelectric and magnetoelastic mechanisms, showing the potential for achieving decoupling perception of multiple physical parameters.

In smart farming and advanced agriculture, drones and robotic manipulators have been increasingly employed to enable image-based assessment of fruit ripeness and autonomous fruit harvesting.[58-59]. However, the sorting of fruits in terms of skin condition, species, etc. may not be easily achieved by the above-mentioned approaches. Herein, by integrating the triboelectric and magnetoelastic effects, a self-powered flexible triboelectric-magnetoelastic tactile sensor with biomimetic anthropomorphic tactile perception (Fig. 1a) was developed to resolve this technical challenge. The triboelectric module featuring pyramid microstructures(Fig. S1(i)) is utilized to detect material type, size and humidity-related tactile information. Meanwhile, the magnetoelastic module possessing a microporous structure(Fig. S1(ii)) is employed to perceive contact force, which leverages its exceptional stability to assist the triboelectric module in suppressing interference. To evaluate the performance of the sensor, it is mounted as electronic skin on a robotic gripper (Fig. 1b), and a convolutional neural network (CNN) algorithm (Fig. 1c) is utilized to identify and classify the materials, pressure and humidity (size was classified by a customized algorithm with gripper motor). The proposed sensor (Fig. 1d) utilizes the bimodal synergistic effect (Fig. 1e) to achieve a recognition accuracy of 99.17% for 60 groups of hybrid multimodal attributes under laboratory conditions (Fig. 1f(i)). To further verify the practical applicability of the sensor, classification tests in intelligent fruit picking scenarios is conducted (Fig. 1f(ii)), and the sensor achieved a favorable recognition accuracy of 98.75% for 8 groups of hybrid attributes including fruit type, size, and humidity-related tactile information. Compared with previous studies on flexible tactile sensors (Table S1), the proposed sensor enables highly robust simultaneous multimodal sensing under self-powered operation. For example, Zheng et al. demonstrated a 44-pixel TENG-based smart insole for high-resolution plantar-pressure mapping, highlighting the effectiveness of

triboelectric arrays for self-powered spatial mechanical sensing[60]. Furthermore, compared with previously reported triboelectric–magnetoelastic tactile sensing systems[61-62], the present work further extends the sensing dimensionality and coupled-state recognition capability. A broader quantitative comparison with representative machine-learning-assisted tactile sensing systems is provided in Table S2 and Note S1. The flexible multimodal sensor developed in this work broadens the tactile perception dimension and recognition accuracy for robotic grippers, showing the great potential for smart farming applications, e.g., autonomous fruit harvesting and sorting robotic system.

2 Experimental Section

2.1 Materials

Polytetrafluoroethylene (PTFE) (nanoscale, 99.9% purity) and fluorinated ethylene propylene (FEP) (nanoscale, 99.9% purity) powders were purchased from DuPont de Nemours, Inc. Single-layer graphene oxide (GO) (flake size 0.2–10μm, 98% purity) was obtained from Shenzhen Suiheng Graphene Technology Co. Polyacrylonitrile (PAN) **(**microscale, 99.9% purity) powder was supplied by Zhonxin Plastic Technology Co.

2.2 Fabrication of the Triboelectric Module

The fabrication process of the triboelectric module is shown in Fig. S2 (i). Firstly, GO, PAN, PTFE, and FEP particles were separately added to isopropanol solution, and then ultrasonic dispersion technology was used to evenly disperse the four types of particles. The A component of Ecoflex00-30 solution was added and the mixture was stirred in a water bath. The filler contents in the final composites were 2 wt% for GO and 4 wt% for PAN, PTFE, and FEP, respectively. After cooling and complete evaporation of isopropanol, the same volume of the B component of Ecoflex00-30 solution was added, and the mixture was stirred with a glass rod for two minutes. The mixture was then poured into a mold with microstructures fabricated via stereolithography 3D printing. The mold was designed with a 1-mm-thick backing layer and 1-mm-high pyramidal features. A vacuum pump was used to remove the bubbles generated during the mixing process. Subsequently, the sample was placed in a 60 °C oven for 1 h to obtain the cured composite block. (Fig. S3). The electrodes and wires were then encapsulated with silicone adhesive.

2.3 Fabrication of the Magnetoelastic Module

The preparation fabrication process of the magnetoelastic module is similar to the triboelectric module, as shown in Fig. S2 (ii). Firstly, neodymium-iron-boron (NdFeB) particles were first mechanically mixed with Ecoflex 00-30 Part B, followed by ultrasonic treatment to further reduce

particle agglomeration and improve dispersion. Then, an equal volume of Ecoflex00-30 A was added, and the mixture was stirred with a glass rod. The mixture was then poured into a mold filled with fine salt particles. A vacuum pump was used repeatedly to remove air to ensure that the silicone gel fully infiltrated the gaps between the salt particles. After curing in an oven, the sample was placed in boiling water to dissolve the salt particles and form a microporous structure. The magnetic response performance was enhanced via high-voltage magnetization using a magnetizer (model MAG, JIUJOK). The customized metal coil and soft magnetic layer were encapsulated with silicone adhesive.

2.4 Sensor Assembly

Once the triboelectric and magnetoelastic modules were independently fabricated, they were assembled to form a hybrid tactile sensor. Firstly, the polyethylene terephthalate (PET) films with the same area as a single triboelectric layer were cut as the isolation material. Nickel cloth with a side length about 1 mm smaller than the triboelectric layer was cut as electrode. Silicone adhesive was applied around PET film to bond the triboelectric layer and complete the encapsulation. The lower surface of the soft magnetic layer was bonded to the metal induction coil with silicone adhesive. Finally, the upper surface of the soft magnetoelastic layer was bonded to the four triboelectric sensing modules with silicone adhesive to complete the overall fabrication of the sensor.

2.5 Fruit Sorting Demonstration

To implement intelligent fruit picking and sorting, the sensor was mounted on a robotic arm (model UR10, Universal Robot) equipped with a two-finger gripper (model CTAG2F90C, ZHIXING). All applied voltage signals were collected by a micro-controller unit (Mega2560, Arduino). The machine learning system based on convolutional neural networks was developed using Python and the Keras and TensorFlow frameworks. The surface morphologies and microscopic features of the triboelectric and magnetoelastic modules were characterized by microscope (model MX-E1, Tuojie Optoelectronic Technology Co.).

2.6 Characterization and Measurements

The relevant experiments of the triboelectric module were measured by an electrometer (model 6514, Keithley) and recorded by an oscilloscope (model MHO3-5004, Micsig). The relevant experiments of the magnetoelastic part were measured by the electrometer and the data were recorded with the help of a signal acquisition card. A linear motor (model BF01-37, Linmot) was used in the frequency, force magnitude and cycle tests. During characterization, humidity control

is achieved by using a humidifier and a sealed box. The sealed box was custom-made from acrylic plates bonded with hot melt adhesive. A humidifier (model WR-J09, Weiruier) was used in the humidity control.

3 Results and Discussion

3.1 Multimodal Sensor Design and Working Principle

The designed sensor structure is shown in Fig. 1d. It integrates a triboelectric sensing module and a magnetoelastic sensing module to achieve synchronous multimodal perception. The top triboelectric module comprises a 2×2 sensing array constructed from four distinct silicone blocks designed with surface microstructures and blended with specific triboelectric fillers (Fig. S1(i)). Operating in the single electrode mode, the array leverages the distinct electron affinities of these four materials to produce unique triboelectric outputs during contact. This differential response mechanism enables the precise recognition of target material properties and surface characteristics. Positioned beneath an isolation layer, the magnetoelastic module consists of a microporous silicone elastomer embedded with magnetic microparticles and a customized planar induction coil (Fig. S1(ii)). Upon the application of external mechanical stimuli, the microporous soft magnetoelastic layer undergoes physical deformation that alters the surrounding spatial magnetic field. According to Faraday's law of electromagnetic induction, this dynamic magnetic flux variation induces a corresponding electrical signal within the underlying coil, thereby facilitating highly sensitive and independent contact force monitoring. The fabrication process and the image of the sensor are shown in Fig. S2 and Fig. S4.

The overall mechanism of the integrated sensor is illustrated in Fig. 1e. In phase (i), when the target object first interacts with the sensor, surface charges are generated due to the triboelectric effect. Because of the relatively large initial distance, only a negligible amount of charge transfer occurs. In phase (ii), as the external object approaches, the electrostatic induction effect alters the local electric field. This variation drives the electron transfer, and generates an accumulation of positive charges on the sensor surface, leading to a preliminary circuit current. During phase (iii), the entire sensor deforms when the external object executes contact pressure. As the distance between the object and the triboelectric layer decreases, extensive electron transfer occurs, and enhances the electrical signal. Meanwhile, the compressive force disrupts the internal magnetic chain structure of the micromagnets within the magnetoelastic body, leading to a reduction in the surrounding magnetic flux density. According to Faraday's law of electromagnetic induction, the planar induction coil accurately detects this variation in the magnetic field, resulting in a corresponding

current output. When the sensor reaches maximum compression in phase (iv), the triboelectric charge reaches saturation, and the electron flow achieves dynamic equilibrium. Moreover, the magnetic flux density on the surface of the magnetoelastic body drops to its lowest value, preventing the generation of induced current. Subsequently, in phase (v), as the external pressure is released, the physical structure gradually reverts to original shape. This recovery causes the electrons to flow in the opposite direction, and generates a reverse current. Simultaneously, the magnetic chain structure of the micromagnets gradually recovers and induces an opposite phase current in the induction coil. Eventually, in phase (vi), during the complete separation of the external object from the sensor, the increasing distance causes the triboelectric layer to undergo reverse electrostatic induction. The system ultimately returns to the stable state observed in phase (i). This complete process demonstrates the ability of the sensor to achieve efficient multimodal perception based on the coordinated interaction of the triboelectric and magnetoelastic mechanisms during the dynamic contact and separation cycle.

3.2 Performance Optimization of the Triboelectric Module

The triboelectric sensing principle is based on the contact electrification phenomenon between materials, which can be explained at the microscopic level by the electron cloud overlap model (Fig. 2a). At the atomic scale, before two materials come into contact, the electron clouds of surface atoms are independent of each other, and electrons are bound by the potential well of the atomic nucleus, with no spontaneous electron transfer due to the extremely high energy barrier for transition. When the two materials are in close contact, the electron clouds significantly overlap and form orbital coupling. Under the action of an external force, the interatomic distance at the



Fig. 1 Triboelectric-magnetoelastic multimodal tactile sensor for intelligent robotic sorting. **a** Human tactile perception neurons and perception functions. **b** Dexterous hand with multimodal sensor. **c** Mixed property classification based on machine learning. **d** Structure of the sensor. **e** Working principle of the sensor. **f** Sensing functions and applications, including (i) mixed tactile perception capability, (ii) smart orchard application.

interface is further compressed, and the potential energy curve changes from a symmetrical single potential well to an asymmetrical double potential well, reducing the energy barrier for electron transition. Eventually, electrons undergo directional cross-interface transfer from the material with lower electron affinity to the one with higher electron affinity. Due to the different electron cloud

states in different materials, the triboelectric signal between two given materials is unique, which endows triboelectric sensors with the ability to recognize materials.

To illustrate the working principle of the single electrode triboelectric sensor, a representative device comprising a PTFE triboelectric layer and a nickel electrode is systematically investigated alongside a tribopositive polyimide (PI) contact material. The dynamic signal generation process is depicted in Fig. 2b. Upon initial physical contact between the two distinct materials, their different electron affinities drive the generation of equal and opposite surface charges (Fig. 2b(I)). During the subsequent separation phase, the disruption of the local electric field balance induces a potential difference. This potential variation drives free electrons to flow from the electrode to the ground, thereby generating an initial output current (Fig. 2b(II)). Once the separation distance reaches its maximum threshold, the electrostatic equilibrium is reestablished and the electron transfer completely ceases (Fig. 2b(III)). Finally, as the target object reapproaches the sensor, the electric field balance is disrupted once again. This physical movement prompts electrons to flow in the reverse direction to neutralize the induced potential (Fig. 2b(IV)), ultimately producing a continuous alternating triboelectric signal across the entire mechanical cycle.

Previous studies have demonstrated that the utilization of microstructures can enhance the signal output amplitude, sensitivity, response speed, linearity of response and service life of flexible sensors[63-65]. To optimize the comprehensive performance of the proposed sensor, a microstructure array was designed on the surface of the triboelectric module. To quantitatively compare the influence of surface geometry on the triboelectric output, four surface configurations (including a flat surface without microstructures, cylindrical, pyramidal, and conical microstructures) were evaluated under controlled normal forces of light load (8N), medium load (16N), and Heavy load (24 N) in Fig. 2c. The mechanical actuation conditions were maintained identical for all measurements, with a complete contact–separation cycle duration of approximately 1.4 s (~0.71 Hz). Each condition was independently repeated five times, and the results are reported as mean ± standard deviation. The output voltage increased with applied force for all four surface geometries. In particular, the pyramidal surface generated 0.2851 ± 0.0069, 0.4220 ± 0.0192, and 0.4780 ± 0.0370 V under 8, 16, and 24 N, respectively, exceeding those of the other surface configurations. When averaged across the three loading conditions, the flat, cylindrical, pyramidal, and conical surfaces produced output voltages of 0.2105, 0.3005, 0.3950, and 0.2699 V, respectively. Consequently, the pyramidal microstructure was selected for the final device. The geometrical parameters of the pyramidal array were selected by considering the balance among microstructure density, deformability, and fabrication reliability within the

stereolithography molding process. A spacing of 2 mm was adopted to maintain sufficient feature density while avoiding excessive mechanical interaction between adjacent elastomeric structures and facilitating reliable mold replication and demolding. The detailed optical images and specific geometric parameters of mentioned 3 microstructures are provided in Fig. S5.

To investigate the relationship between the operating parameters of a single triboelectric unit and the signal output, a test platform based on a linear motor was set up (Fig. S6). Firstly, the size of the sensor affected the amplitude of the voltage, as a larger triboelectric layer size carried more surface charge and transferred more charge during operation (Fig. S7). Additionally, the distance of contact and separation also influenced the value of Voltage. When the sensor was 5-20 mm away from the object being measured, Voltage gradually increased, and remained almost unchanged when the distance exceeded 20 mm (Fig. 2d). The operating frequency exhibited a non-negligible influence on the signal output (Fig. 2e), possibly because changes in operating frequency alter the contact–separation velocity and the time available for surface-charge relaxation and dissipation. As the contact force increased from 5 to 25 N, the amplitude of the output sensing signal increased substantially and steadily, with the maximum peak amplitude rising by more than 300% (Fig. 2f). A comprehensive electrical characterization of the four triboelectric sensing channels, including short-circuit current, transferred charge, effective transferred charge density, load-dependent output, effective matched load resistance, energy delivered per cycle, and peak power density, is provided in Fig. S8 and Note S2. Under the common working environment of the sensor, temperature had a relatively small impact on the sensing signal. The signal variation was controlled within 10% when the temperature changed from 25°C to 50°C (Fig. 2g). However, humidity had a very significant effect on the sensing signal. In the humidity range of 50% relative humidity (RH) to 80% RH, the signal amplitude decreased significantly with increasing humidity, with a maximum reduction of up to 80% (Fig. 2h). The sensor maintained signal stability after repeated use in a laboratory environment. After 10,000 continuous loading cycles, the triboelectric module maintained a stable output without obvious signal-amplitude attenuation or baseline drift (Fig. 2i), demonstrating good cycling durability under the continuous operating conditions. Additional characterization of the four filler/Ecoflex triboelectric composites and the 2 × 2 sensing array is provided in the Supporting Information (Note S3 and Figs. S9–S10). In summary, TENG has the characteristics of simple structure, strong adaptability, and good cycle stability, but external force and humidity both have a significant impact on its performance.

Benefiting from the nearly linear negative correlation between humidity and the sensing signal, expanding a single TENG unit into an array can decouple humidity. Relevant studies have

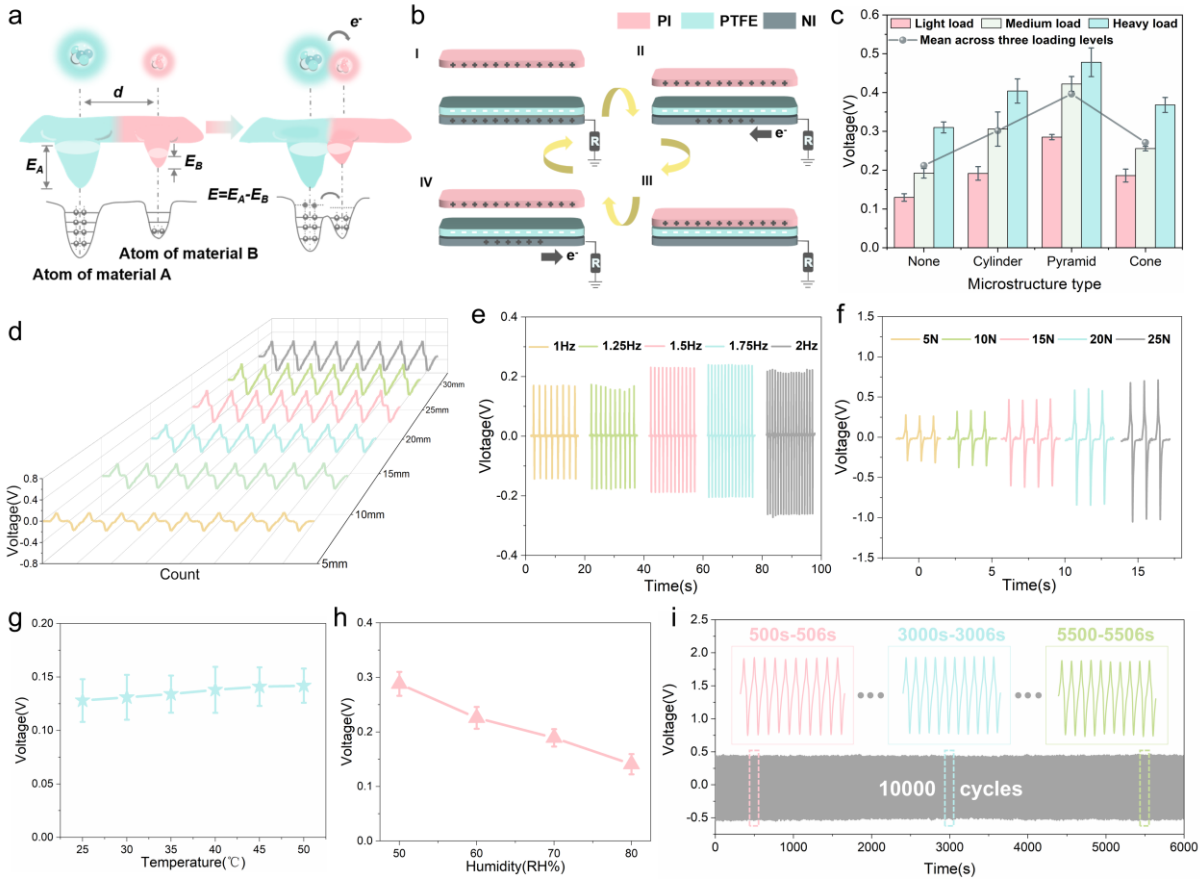


Fig. 2 Working mechanism of the triboelectric module and its performance characterization. **a** Electron cloud model of the triboelectric sensing. **b** Working mechanism of single-electrode TENG. **c** Output comparison between different microstructures. **d** Voltage at different contact distances. **e** Influence of working frequency on TENG output. **f** Influence of contact force on TENG output. **g** Voltage output at different operating temperatures. **h** Voltage output at different operating humidities. **i** Fatigue test of the triboelectric module over 10,000 loading cycles.

demonstrated that GO has strong sensitivity to humidity and some humidity sensors have been fabricated based on this principle[66-67]. Therefore, GO and three other powdered materials were blended into the silicone substrate to form a 2×2 sensing array (Fig. 3a). These materials, specifically PAN, PTFE, and FEP, were strategically selected from both the positive and negative regions of the triboelectric series. Different combinations of triboelectric layers with different blended materials can obtain more comprehensive characteristic information of the measured object, thereby effectively improving the recognition accuracy.

The structure of the triboelectric module is shown in Fig. 3a. The arrayed sensing modules generate distinct electrical signals when the target object contacts and subsequently separates from the sensor. The collected voltage signals are initially processed by a customized circuit for lowpass

filtering and amplification (Fig. S11). Subsequently, these refined signals are acquired by a microcontroller unit (MCU) and transmitted to a computer serial port for further analysis (Fig. 3b). The triboelectric module is used to identify the size, material and humidity of objects. For two objects that differ in size but are the same in material and humidity, when a gripper grasps a single object twice, two triboelectric signals that are almost the same in shape but only differ in time sequence will be generated. The time difference between the first triboelectric signal and the second triboelectric signal is recorded as t. Notably, the value of t has a certain relationship with the size of the object. Specifically, the larger t is, the smaller the size of the object. This is because when two objects come into contact, the transferred charge reaches its peak, thus generating a voltage extremum. When the operation parameters of the gripper for two grasps are the same, the smaller the object size, the longer the travel distance. The difference in distance leads to a difference in the time t when the object to be grasped is touched. As shown in Fig. 3c, all four channels exhibit this pattern. Taking the PAN channel as an example, t_1, t_2 and t_3 are the time differences between the first extremum signals of adjacent working cycles when grasping large, medium and small objects, respectively. In terms of value, $t_1 < t_2 < t_3$ corresponds to object 1 size > object 2 size > object 3 size, which is consistent with the previously explained pattern. By using this pattern, the size of the object can be identified without additional complex constraints or algorithms.

To evaluate the material recognition capability of the triboelectric module, grasping experiments were conducted using five distinct materials including terylene, leather, nickel cloth, PI, and polycarbonate (PC). Different materials generate distinct signals in the array channels (Fig. 3d). Taking PC as an example (Fig. 3f), the silicone-based sensing units blended with GO, PAN, PTFE, and FEP all produced similar "positive first, then negative" voltage output signals. This is because the PC possesses a lower electron affinity than the silicone sensing units blended with GO, PAN, PTFE, and FEP, which locates PC in the tribopositive region of the triboelectric series. Notably, the maximum and minimum values of the output signals from the triboelectric sensing units vary, which is attributed to the differences in their abilities to gain and lose electrons. Compared with other channels, the silicone-based triboelectric sensor blended with FEP is more inclined to gain electrons, thus having the largest triboelectric output amplitude, followed by those blended with PTFE and PAN. Since both GO and PC are in the more positive region of the triboelectric series and have similar abilities to gain and lose electrons, the voltage output amplitude of the triboelectric sensing unit blended with GO is the smallest. This rule can be utilized to achieve the multi-material recognition function of the triboelectric module.

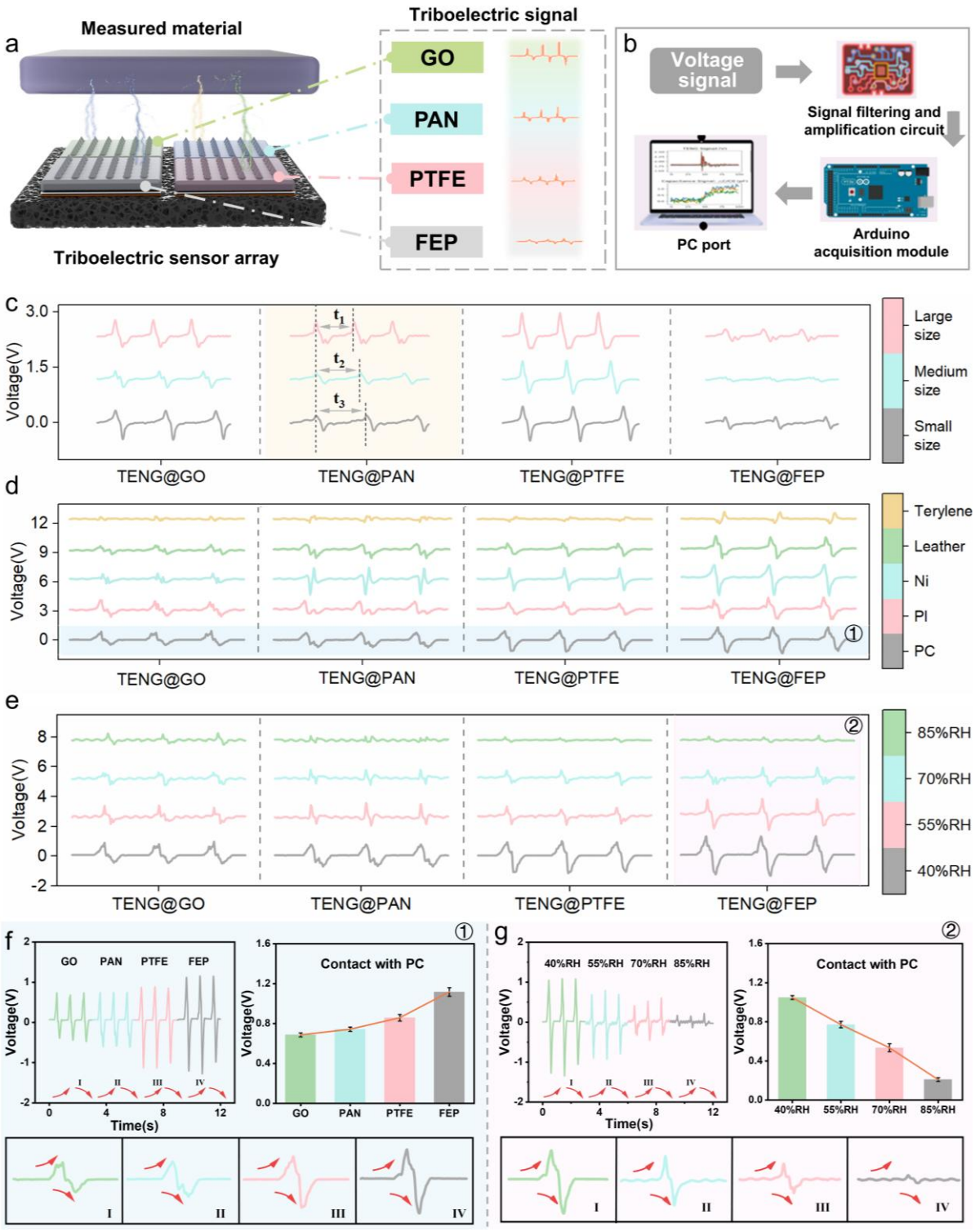


Fig. 3 Identifications of various contact features via the triboelectric array. **a** Schematic diagram of the triboelectric array. **b** Voltage signal processing methods. **c-e** The voltage waveforms and amplitudes output when the sensor array identified size, material, and humidity. **f** Material recognition method. **g** Humidity recognition method.

For the humidity recognition capability of the triboelectric module, relative humidity ranging from 40% to 85% were selected and divided into four levels for testing (40% RH, 55% RH, 70% RH, and 85% RH). Different humidity levels caused significant amplitude changes in the array channels (Fig. 3e). Taking the sensing unit blended with FEP in the array as an example (Fig. 3g), when in contact with PC, it can be observed that the overall signal polarity and waveform characteristics remained similar, whereas the signal amplitude decreased with increasing RH. This is because the material in contact is the same. Notably, the maximum and minimum values output by each triboelectric sensing unit vary. This is due to the enhanced adsorption of water molecules at the triboelectric interface facilitates surface-charge dissipation and modifies the effective contact-electrification process. Therefore, for a single FEP unit in contact and separation with the same material, a voltage exceeding 1V can be generated at low humidity (40% RH), but the voltage signal drops significantly as humidity increases (0.2V at 85% RH). This rule can be utilized to identify the humidity on the surface of an object. Additional characterization of the humidity response time, recovery time, cycling and temperature dependence is provided in Fig. S12 and Note S4. In addition, surface wettability is an important factor governing water–solid interfacial interactions, and the water contact angle provides a direct macroscopic measure of the hydrophilic/hydrophobic characteristics of a material surface[68]. Therefore, static water contact angle measurements of four triboelectric composite surfaces were also carried out, as described in Fig. S13 and Note S4.

3.3 Performance Optimization of the Magnetoelastic Module

The structure of the magnetoelastic module is shown in Fig. 4a, which consists of a magnetoelastic layer and a metal induction coil layer. The dynamic working principle of the independent magnetoelastic sensing module is systematically illustrated in Fig. 4b. The energy conversion process consists of four distinct functional stages designated as separating, pressing, suspending, and releasing. In the initial state(i), the embedded magnetic microparticles maintain a stable wavy chain structure within the elastomeric matrix. The surrounding spatial magnetic flux density remains constant, resulting in zero induced current in the underlying planar coil. During the subsequent pressing stage(ii), the application of an external mechanical force physically compresses the soft structure. This deformation disrupts the internal magnetic chains and consequently alters the local magnetic field. According to Faraday's law of electromagnetic induction, this dynamic magnetic flux variation instantaneously induces a corresponding electrical current within the coil. When the system enters the suspending stage(iii), the structural

compression reaches its absolute maximum and remains static. At this point, the magnetic flux density stabilizes at its minimum value, and prevents any further generation of induced current. Finally, in the releasing stage(iv), the removal of the external pressure allows the matrix to elasticalrevert to its original dimensions. The internal magnetic chain structure gradually recovers to restore the magnetic flux to its initial level. This reverse dynamic process induces an opposite current in the metal coil before the entire device ultimately returns to the stable original state.

By comparing the current generated by the microporous structure (Fig. 4a(i)) and the solid structure (Fig. 4a(ii)) of the magnetoelastic material under an applied force ranging from approximately 1 to 28 N (Fig. 4c), it was found that the difference in the induced current was insignificant under small force (1N-6N). However, as the force gradually increased (6N-28N), the microporous structure exhibited a significant advantage, and this advantage became more pronounced with increased external force. At 28N, the induced current generated by the microporous structure was more than twice that of the solid structure. The reason for this phenomenon is that the induced current is positively correlated with $d\Phi/dt$. The stiffness of the magnetoelastic material with a porous structure is much smaller than that of the solid structure, leading to a larger deformation under the same external for and a greater change in the magnetic field.

To further optimize the output performance of the magnetoelastic material under low pressure, three parameters, i.e., the thickness of the magnetoelastic layer, the mass ratio of the NdFeB micromagnets, and the design of the metal induction coil, were selected for optimization. As shown in Fig. 4d, the thickness of the magnetoelastic layer was positively correlated with the output current. When the thickness increased from 2 mm to 3 mm and from 3 mm to 4 mm, the output current increased by approximately 50% each time. When the thickness increased from 4 mm to 5 mm, the output current increased by about 20%. Considering the volume and portability of the sensor, a thickness of 4 mm was chosen. The signal of a single working cycle at a thickness of 4 mm is shown in Fig. 4e. Under external force, the compression and rebound each presented a half-cycle signal with opposite phases in one complete working cycle. For the mass ratio of NdFeB, the ratios in the range of 30% to 50% with an increment of 5% were studied (Fig. 4f). The results showed that the peak output current increased with the increase of the blending mass ratio, exhibiting a clear positive linear correlation. Theoretically, increasing the blending ratio can obtain a larger signal output. However, further increasing the NdFeB powder will seriously affect the mechanical system of the silicone rubber substrate, leading to substrate cracking and inability to rebound. Therefore, a blending mass ratio of 50% was finally selected.

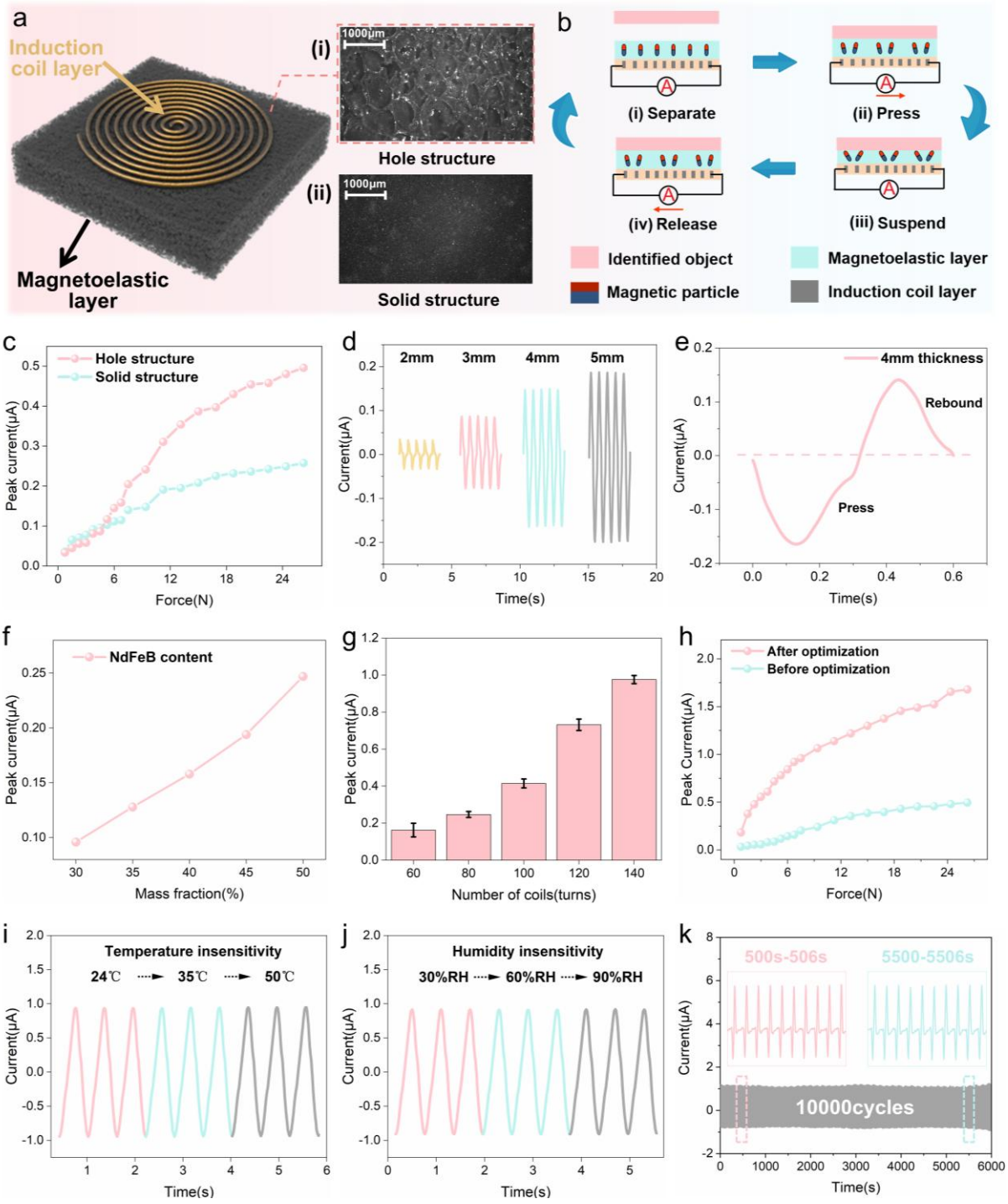


Fig. 4 Mechanism of magnetoelastic module and its performance characterization. **a** Structure of the magnetoelastic module, including (i) microporous structure, (ii) solid structure. **b** Working principle of the magnetoelastic module. **c** Output comparison between the solid structure and the microporous structure. **d** Influence of magnetoelastic layer thickness on the output performance. **e** Output signal of a complete working cycle obtained from the 4 mm-thick magnetoelastic layer. **f** Influence of NdFeB content on the peak output current. **g** Effect of induction coil turn number on device output performance. **h** Output comparison before and after optimization of the

magnetoelastic module. **i** Temperature stability test. **j** Humidity stability test. **k** Fatigue test of the magnetoelastic module over 10,000 loading cycles.

For the design of the metal induction coil, parameters such as coil diameter, line width, and number of turns were considered. Regarding the number of turns, when 60 to 140 turns were selected as the research objects with an increment of 20 turns, it was found that the peak current increased with more turns. Notably, the current output increase from 100 to 120 turns was about 40%, while the increase from 120 to 140 turns was only about 20%. This indicates that the optimal range of the coil is around 120 turns. When the number of turns continues to increase, the negative effects such as coil resistance, inductive reactance, and noise may exceed the electromotive force gain brought by turn number, causing the output current growth rate to slow down or even decrease. Therefore, 120 turns were finally chosen for the metal induction coil (the other parameters of the coil are shown in Table S3). It should be emphasized that the above parameters were not selected by independently maximizing the electrical output of the MEG, but through an integrated design considering output performance, device thickness, mechanical deformability and elastic recovery, and compatibility with the upper TENG array. Increasing the magnetoelastic-layer thickness improves the induced current, but simultaneously increases the overall device thickness and deformation resistance. In particular, the output enhancement decreased to only approximately 20% when the thickness was further increased from 4 to 5 mm, indicating a clear diminishing return. Similarly, although a higher NdFeB content enhances the magnetic response, excessive particle loading compromises the mechanical integrity and elastic recovery of the silicone matrix. Increasing the coil turns also improves the induced output, but the incremental gain becomes progressively smaller beyond 120 turns while additional resistance, inductive reactance, and noise are introduced. Therefore, the final combination of a 4-mm magnetoelastic layer, 50 wt% NdFeB content, and a 120-turn coil was selected as a balanced configuration that provides sufficient MEG output for mechanical sensing and multimodal decoupling while maintaining the compactness and deformability required for integration with the triboelectric module. After completing the optimization of the magnetoelastic module, it was found that the peak current output was significantly improved at all stages under the same force range of 1N to 28N (Fig. 4h). At 28N, the peak current increased by about four times.

When the magnetoelastic module is used for force sensing and auxiliary decoupling, its environmental adaptability and working stability must be fully considered to avoid introducing new coupling relationships due to the addition of a sensing mechanism. For this purpose, tests on temperature, humidity, and cyclic stability were conducted. The magnetoelastic module

demonstrated excellent stability within the temperature range of 24 °C to 50 °C, indicating that it is not affected by the temperature of the object (Fig. 4i). Similarly, under a wide humidity range from 30% RH to 90% RH, the magnetoelastic module maintained excellent stability, indicating that it is not affected by the humidity of the target object (Fig. 4j). During the fatigue test, the magnetoelastic module maintained a stable current output after 10,000 continuous loading cycles, with no obvious attenuation in signal amplitude or baseline drift (Fig. 4k), confirming its good cycling durability under the tested conditions.

3.4 Feature Recognition via Machine Learning

The triboelectric module provides material-, humidity-, and loading-dependent information, whereas the magnetoelastic module introduces a complementary mechanical information dimension. Their complementary response mechanisms and interference transmission pathways are further analyzed in Supplementary Note S5 and Fig. S14. To extract the discriminative features embedded in these coupled multimodal signals, the synchronized TENG and MEG outputs from the integrated triboelectric–magnetoelastic sensor (Fig. 5a) were subsequently fused and processed using a CNN to achieve multidimensional feature extraction and decoupling. For the four-channel signal acquisition method of the triboelectric module, the voltage signal was collected by an MCU after processing by a filter circuit, and the current signal of the magnetoelastic module was collected by an electrometer connected with a signal acquisition card. For the two heterogeneous acquisition systems, timestamp alignment, clock-drift compensation, sampling-rate unification, and data fusion were implemented programmatically, and a standard machine-learning dataset with a consistent sampling rate and five-channel column storage was subsequently generated (Fig. 5b). The output form of the five-channel signal is shown in Fig. 5c. Here, taking the change in grasping force and keeping other factors constant as an example, it can be seen that although the signal amplitude of the triboelectric module changes under the influence of force, the amplitude is not as obvious and stable as that of the magnetoelastic module, which once again proves the advantage of the magnetoelastic module in force perception and decoupling.

Although the unique features of the electrical output signals from triboelectric-magnetoelastic hybrid sensor have been verified to act as an initial method for object property identification, these properties are often multi-dimensional and coupled, which greatly increases the difficulty of manual feature extraction. Therefore, in order to achieve more accurate and comprehensive identification of object properties, a deep learning algorithm was introduced to automatically extract deep-level features and it can efficiently and accurately classify materials, humidity, and

force. Here, a convolutional neural network was chosen to develop an object property recognition model, whose framework diagram is shown in Fig. 5d. The model includes two groups of convolution-pooling layers and a fully connected layer. The first group of convolution-pooling layers is used for initial feature extraction and feature optimization, while the second group of convolution-pooling layers is used for further refinement and extraction of complex features and reduction of data dimensions to highlight key features. The fully connected layer flattens the data, comprehensively processes the previously extracted features, and outputs the classification. The comprehensive experimental platform is shown in Fig. S15, where a robotic gripper equipped with the tactile sensor was used to grasp the object in a closed transparent acrylic space. Moreover, the grasping force was controlled by adjusting the driving current of the gripper, and the humidity was controlled by the humidity controller. The material recognition capability was verified by changing the object to be identified. The feature recognition variables include 5 materials, 4 humidity levels, and 3 forces, totaling 60 combinations. For each of the 60 material–humidity–force classes, 100 independent samples were collected, resulting in a total dataset of 6000 samples. For each class, 60 samples were used for training, 20 for validation, and 20 for testing, corresponding to a 60:20:20 split. Therefore, the complete dataset contained 3600 training samples, 1200 validation samples, and 1200 test samples. The corresponding feature variables for each combination are shown in Table S4. When only the triboelectric module was used to decouple and classify the materials and humidity, an accuracy rate of 96.25% was achieved (Fig. S16). When three different force levels were introduced as additional variables, the recognition accuracy of the triboelectric module alone decreased to 94.25% (Fig. 5e), indicating that force-induced variations in the triboelectric signals introduced additional feature coupling and impaired classification performance. At this point, if the current data brought by the magnetoelastic module was added, the accuracy rate rose to 99.17% (Fig. 5f), suggesting that the magnetoelastic module not only accurately identified the force but also played an auxiliary decoupling role. To explicitly visualize this decoupling superiority introduced by the magnetoelastic module, the classification strategy was intentionally restricted to 20 categories combining material type and RH condition. The three varying contact forces were deliberately embedded as hidden variables within these specific categories. The subsequent t-SNE visualizations reveal distinct clustering behaviors. For the standalone triboelectric module, the feature distribution demonstrates noticeable variability. While certain specific categories successfully separate into three distinct clusters responding to the varying forces, multiple other categories merge into a single overlapping group (as depicted by the clusters marked with ellipses in Fig 5e). This partial separation phenomenon indicates that although the triboelectric mechanism possesses certain force sensitivity, the uncalibrated contact forces still significantly confound the

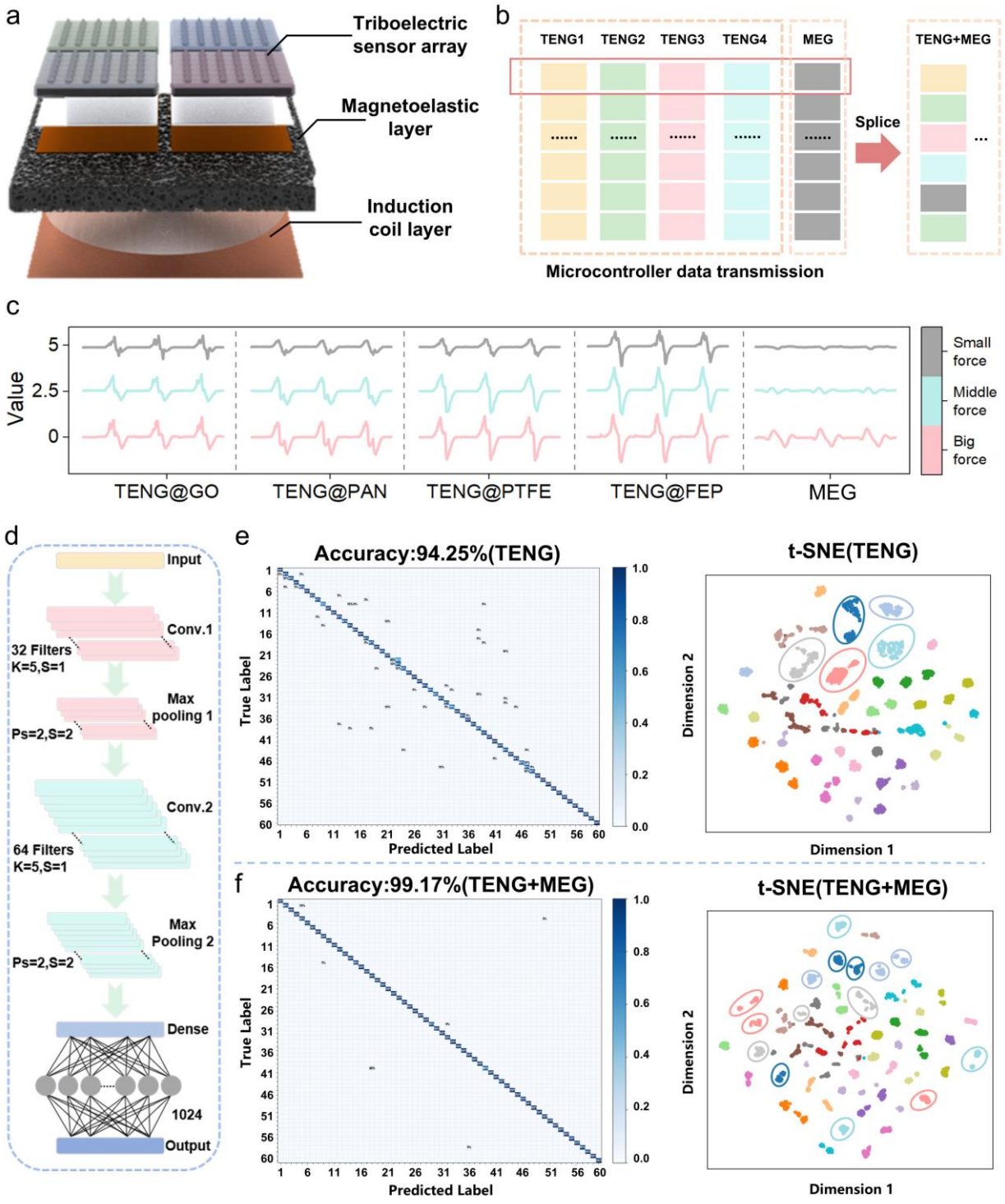


Fig 5. Feature recognition method and results. **a** Overall structure diagram of the sensor. **b** Signal merging of triboelectric and magnetoelastic. **c** The overall sensor signal (five channels). **d** Schematic diagram of the CNN network. **e, f** Recognition results for 60 combined states involving materials, forces, and humidity, including confusion matrices and t-SNE visualizations comparing the TENG module and the integrated TENG and MEG modules.

intrinsic material and humidity characteristics across different conditions. Conversely, the integrated hybrid system demonstrates improved feature separability. Within the boundary defining each specific material and humidity combination, the data points systematically partition into three distinct sub clusters (Fig 5f, including the clusters in Fig 5 that fail to partition into three distinct groups). These three sub clusters perfectly correspond to the three embedded force variations. This unsupervised natural separation strongly verifies that the magnetoelastic module introduces a complementary mechanical-information dimension, enabling high precision feature extraction robust against dynamic physical fluctuations. Additionally, the CNN model outperformed the artificial neural network (ANN) and support vector machine (SVM) models in classifying the coupled states (Fig. S17). This phenomenon can be primarily attributed to the force-dependent deformation of the flexible TENG microstructures, which alters the effective contact area and interfacial contact configuration. Consequently, material, humidity, and mechanical loading are simultaneously encoded in the same TENG responses, and different physical states may exhibit partially overlapping feature distributions when only the TENG signals are available. Although CNN-based feature extraction can reduce such ambiguity, it has limited ability to fully distinguish different physical states when the underlying TENG responses themselves are similar. In contrast, the MEG channel provides an additional mechanical-information dimension, enabling force-induced variations to be distinguished more effectively from material- and humidity-dependent triboelectric responses. Taken together, these results demonstrate that the hybrid sensor, assisted by CNN-based feature learning, enables accurate and robust decoupling of material, humidity, and force under varying contact-force conditions.

3.5 Intelligent Fruit Picking and Sorting Applications

The utilization of robotic gripper to perform fruit picking and sorting on fruit trees is a key point for achieving smart orchard management in the future. The robotic gripper with triboelectric-magnetoelastic sensor was harnessed to sense the material, size, and relative humidity of the picked fruit and control the picking force. After grasping, the fruit attributes were further identified and classified (Figs. 6a and 6b), and the fruits were subsequently sorted into the corresponding logistics categories according to the recognition results. The tactile recognition method for fruit size is achieved by determining the time interval between the first peak values of two triboelectric working cycles. This implies that the fruit must be grasped at least twice to identify its size. However, multiple grasps not only reduce the picking efficiency but also increase the damage rate of the fruit during the grasping process. Therefore, the size recognition method has been optimized as shown in Fig. 6c. The on-off state of the gripper motor current was acquired to determine its

operating status, which was used to synchronize the trigger timing of signal acquisition for the triboelectric-magnetoelastic multimodal sensor. The first peak of the triboelectric signal was replaced with a timestamp triggered by the high level of the motor current. In this way, the first peak generated when the triboelectric-magnetoelastic sensor first contacted the target object was recorded as the second timestamp, enabling tactile information perception of the target object with only one touch. The reference threshold t_0 was calibrated by pre-grasping a standard block under the same operating conditions. The gripper was initialized from the same opening state, operated at a constant closing speed. Under these fixed conditions, t reflects the effective grasping dimension along the gripper-closing direction, and t_0 serves as a setup-specific threshold. In subsequent experiments, objects with $t>t_0$were classified as small, whereas those with $t<t_0$were classified as large. In this way, the effective grasping dimension of the target object can be determined within a single grasping operation. To further validate the applicability of this optimized single-touch strategy across different fruit species and surface characteristics, additional experiments were conducted using three previously untested fruits (Note S6, Fig. S18 and Table S5). For the identification of fruit type and RH condition, a CNN algorithm was used for refined classification, where the magnetoelastic module was used for auxiliary decoupling. Four types of fruits (apple, orange, tangerine, and lemon) and two humidity levels (30% RH and 65% RH) were selected, resulting in a total of eight hybrid attribute groups for recognition. The gripped signals are shown in Fig. 6b, and it can be found that the signals with high humidity are generally low, and the TENG signals generated by different fruit varieties have differences in polarity and amplitude. These differences in signal characteristics are conducive to the distinction of material and humidity, and are consistent with previous analysis.

For the 8 types of fruits, the confusion matrix accuracy, clustering plot and loss plot obtained by deep learning are shown in Fig. 6d, Fig. 6e and Fig. S19 respectively. The training loss decreased to approximately 0.01 after 60 epochs, while the validation loss stabilized at approximately 0.09. The corresponding training and validation accuracies converged to approximately 100% and 98%–99%, respectively, with no evident divergence observed during further training. In the t-SNE clustering plot, the clustering clusters of the targets are compact and well-separated with few intra-class samples dispersed and no significant overlap between different classes, indicating that the feature extraction effect meets the expectations and the model can effectively distinguish the feature differences of different targets. The confusion matrix shows that the proportion of correct classification on the main diagonal reaches 98.75%, indicating that the classification effect meets the expectations. To further evaluate the adaptability

of the system to representative non-ideal orchard conditions, additional tests involving surface particulate contamination and variations in fruit geometry and grasping orientation were performed (Fig. S20). These results demonstrate that the proposed tactile sensing system possesses a certain tolerance to surface particulate interference. The orientation tests indicated stable size categorization for fruits with relatively regular geometries, while for highly irregular fruits, integrating tactile sensing with visual perception may further improve size determination and grasping accuracy. Detailed experimental results and discussion are provided in Note S7 and Fig. S20. To further evaluate the reproducibility of the fruit-classification performance beyond the original dataset, two independently fabricated sensors were evaluated using two additional batches of newly collected fruit specimens belonging to the same eight fruit type classes. Sensor 1/Fruit Batch 1 achieved accuracies of 95.00% and 98.13% using TENG-only and fused TENG–MEG signals, respectively, whereas the corresponding accuracies for Sensor 2/Fruit Batch 2 were 93.75% and 97.50% (Fig. S21, Note S8 and Table S6). Thus, incorporation of the MEG channel improved the classification accuracy by 3.13 and 3.75 percentage points in the two independent validations, respectively. These results support the reproducibility of the performance enhancement provided by the hybrid sensing architecture across the tested devices and fruit batches.

A simulated orchard scenario was constructed to verify the comprehensive recognition ability of the designed triboelectric-magnetoelastic sensor for materials, force, relative humidity and size in intelligent fruit picking. The schematic workflow and experimental scene are shown in Fig. 6f. This scene includes a robotic arm and a robotic gripper for performing fruit picking and sorting tasks, the multimodal sensor, and a humidity controller. Notably, to simulate diverse humidity conditions within the same scenario, water mist generated by the humidity controller was utilized to establish a localized high humidity environment. The fruit sorting process is shown in Fig. 6h. To prevent fruit damage, the pre-grasping force was set to a relatively low level. After the pre-grasping action was completed, the relevant signals were immediately collected by the data acquisition system composed of an MCU and a signal acquisition card. After comprehensive processing and integration, these signals were transmitted to the processing system on the laptop via a communication channel and they were further analyzed using the aforementioned CNN algorithm to obtain fruit type and humidity information. Additionally, combined with the current signal of the gripper, high-accuracy decoupled information of the grasped fruit including type, relative humidity, size, and contact force was obtained. With the simple network architecture and the low complexity of the lightweight convolutional neural network algorithm, the system can

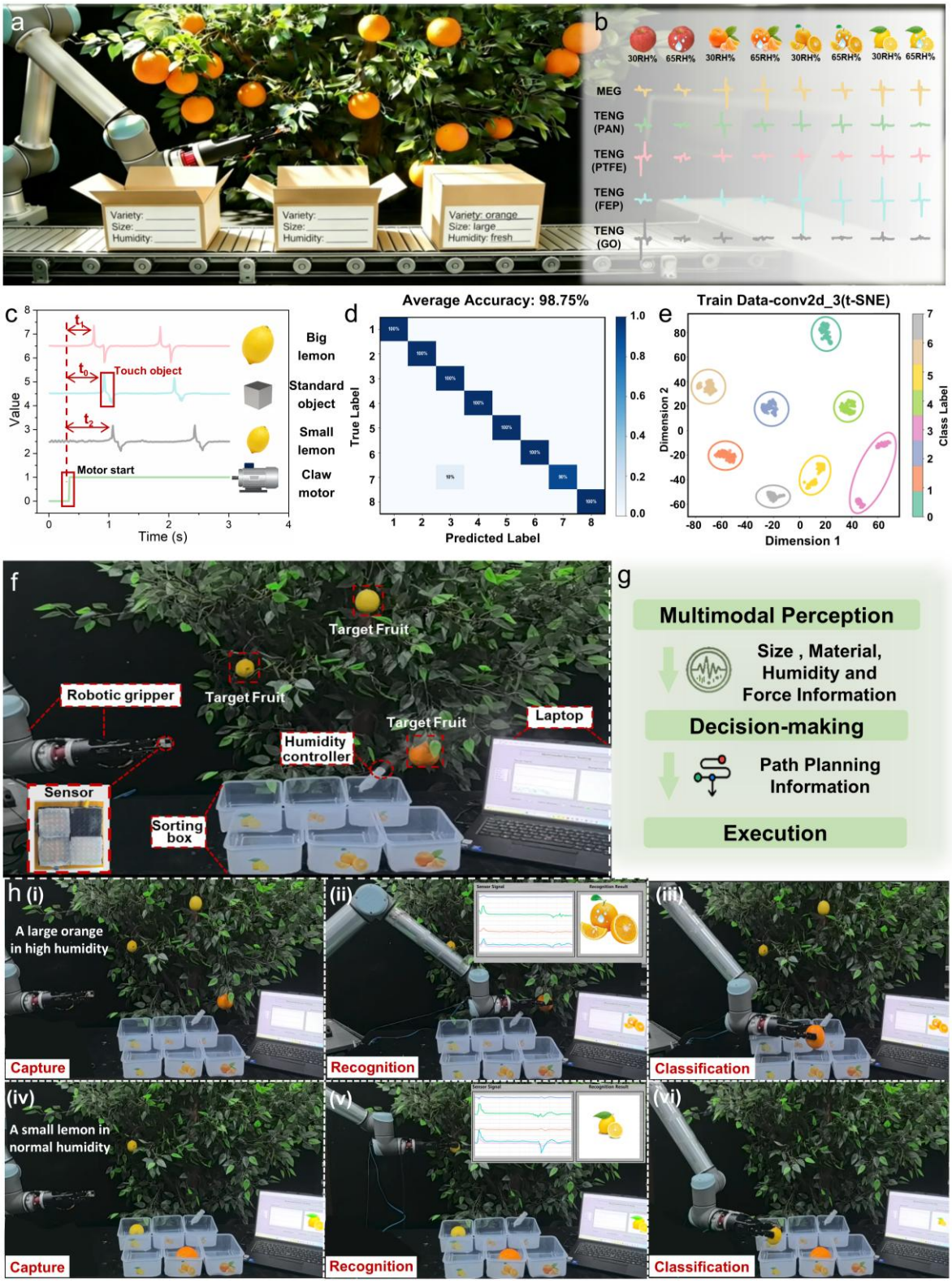


Fig. 6 Demonstration of intelligent fruit picking and sorting applications. **a** Conceptual diagram for automated fruit picking and sorting scenarios. **b** Feature signal representation for multi-attribute fruit characterization. **c** Real-time signals for fruit size estimation. **d, e** Confusion matrix and clustering plot for fruit attributes classification. **f** Illustration of robotic fruit harvesting. **g** Schematic workflow of intelligent fruit picking and sorting **h** Fruit picking experiment, including

(i, iv) robotic capturing execution, (ii, v) real-time fruit attribute identification, (iii, vi) attribute-based sorting and classification.

complete a single inference task and display the signal and classification results in real time on the laptop without noticeable computational delay (<4ms) during the fruit-sorting process. After the recognition was completed, a second grasping action was performed. Since the fruit attributes had been identified, the grasping force was adjusted during this step to ensure safe grasping and transportation of the fruit. The fruit was transported to the position above the corresponding classification box (pre-programmed via the robotic arm's teaching function), released, and the gripper returned to the initial position. For instance, Fig. 6h (i to iii) illustrates the recognition process regarding a large orange within high humidity environment, whereas Fig. 6h (iv to vi) presents the identification procedure for a small lemon under normal humidity conditions. The robotic classification outcomes confirm that the sensor successfully achieves accurate recognition in both scenarios. The individual classification demonstrations targeting fruit variety, relative humidity, and object size are presented in supplementary videos 1, 2, and 3. Furthermore, the comprehensive classification scenario is illustrated in supplementary video 4.

4 Conclusions

In summary, this work presents a self-powered multimodal tactile sensor consisting of a triboelectric module and a magnetoelastic module for robotic gripper to overcome the signal coupling and force-induced interference via conventional flexible sensors in fruits sorting tasks. The triboelectric module has a 2×2 sensory array based on single-electrode mode TENG, where triboelectric materials with distinct electronegativities are constructed via blending powder materials into silicone substrates. Based on Faraday's law of electromagnetic induction, the magnetoelastic module utilizes a microporous elastomer to enlarge its output, and the electrical performance is further optimized by parameters including elastomer thickness, NdFeB microparticle mass ratio, and the coil parameters. Subsequent evaluations across different temperature, humidity, and cyclic conditions verify the exceptional environmental robustness for this module. Powered by a customized convolutional neural network, the triboelectric array achieves accurate recognition for material type and relative humidity condition, while magnetoelastic module endows the system with grasping force perception to eliminate the interference caused by contact force variations on the triboelectric signals. Hence, the hybrid sensor improves the comprehensive recognition accuracy for object size, material, grasping force, and humidity. It is validated to achieve a remarkable recognition accuracy of 99.17%

across 60 hybrid attribute groups under laboratory conditions, outperforming the single triboelectric sensor by 4.92%. On this basis, the intelligent robotic fruit sorting is demonstrated after mounting the multimodal sensor onto a robotic gripper, and it delivers an outstanding 98.75% classification accuracy across complex operations involving 8 coupled attributes. Afterward, the system successfully completed the fruit picking and classification work under variable environmental conditions in the simulated orchard scenario. The robotic gripper with such triboelectric-magnetoelastic hybrid sensor exhibits an additive enhancement and reveals deep-level information, offering a valuable path toward autonomous fruit harvesting in smart farming applications.

Acknowledgments

We acknowledge the support from the National Natural Science Foundation of China (grant nos. 62303291, 62473244, and 62273222), the Foundation of Science and Technology Commission of Shanghai Municipality (grant nos. 24511103800, and 24TS1402300), the Shanghai Natural Science Foundation (Grant No. 25ZR1402155) and Open Project of National Key Laboratory of Aerospace Mechanism (grant no. 2024ASM-KFYB06).

Authors' Contributions: C. Z., L. X., and X. L. contribute equally to this work. C. Z., L. X., and X. L. conceived the idea, fabricated the device, conducted the experiment, collected and analyzed the data, constructed the deep learning model, rendered the figures, and wrote the manuscript. M. F., X. B., Y. T., and L. L. participated in the experiment and research. T. J., Y. L., and C. L. guided and supervised this work.

Declarations

Conflict of Interest The authors declare that they have no known competing financial interests or personal relationships that could have appeared to influence the work reported in this paper.

References

[1] S. Zhang, Y. Yang, Y. Sun, N. Liu, F. Sun et al., Artificial Skin Based on Visuo-Tactile Sensing for 3d Shape Reconstruction: Material, Method, and Evaluation. Adv. Funct. Mater. **35**(1), 2411686 (2024). https://doi.org/10.1002/adfm.202411686

[2] L. Zhuang, X. Zhong, L. Xu, C. Tian, and W. Yu, Visual Slam for Unmanned Aerial Vehicles: Localization and Perception. SENSORS-BASEL **24**(10), 2980 (2024). https://doi.org/10.3390/s24102980

[3] Y. Xie, H. Cheng, C. Yuan, L. Zheng, Z. Peng et al., Deep Learning-Assisted Object Recognition with Hybrid Triboelectric-Capacitive Tactile Sensor. Microsyst. Nanoeng. **10**(1), 165 (2024). https://doi.org/10.1038/s41378-024-00813-2

[4] X. Qu, Z. Liu, P. Tan, C. Wang, Y. Liu et al., Artificial Tactile Perception Smart Finger for Material Identification Based on Triboelectric Sensing. Sci. Adv. **8**(31), eabq2521 (2022). https://doi.org/doi:10.1126/sciadv.abq2521

[5] K. Tao, J. Yu, J. Zhang, A. Bao, H. Hu et al., Deep-Learning Enabled Active Biomimetic Multifunctional Hydrogel Electronic Skin. ACS Nano **17**(16), 16160 (2023). https://doi.org/10.1021/acsnano.3c05253

[6] Q. Nie, F. Wang, F. S. Yang, H. Xun, J. Hou et al., Intelligent Tactile Perception Revolution: Innovations in Flexible Fet-Based Tactile Sensors for Next-Gen Human-Machine Interfaces. Adv. Mater. **38**(10), e10646 (2026). https://doi.org/10.1002/adma.202510646

[7] B. Wang, D. Kong, H. Yang, K. Xu, and G. Yang, Ai-Powered Electronic Skin: From Smart Design to Cognitive Interaction. Bio-Des. Manuf. **9**(1), 4 (2026). https://doi.org/10.1631/bdm.2500376

[8] X. Hu, Z. Liu, and Y. Zhang, Three-Dimensionally Architected Tactile Electronic Skins. ACS Nano **19**(15), 14523 (2025). https://doi.org/10.1021/acsnano.5c02232

[9] C. Yifan, M. Wei, X. Wang, Y. Liu, J. Wang et al., Embodied Ai: A Survey on the Evolution from Perceptive to Behavioral Intelligence. SmartBot **1**(3), e70003 (2025). https://doi.org/10.1002/smb2.70003

[10] C. Wu, Y. Peng, S. Wang, B. Qiu, G. Li et al., Hierarchical Structural Design Towards Stretchable Strain Sensors with Ultra-High Sensitivity and Linearity. Science China Materials **67**(7), 2319 (2024). https://doi.org/10.1007/s40843-024-2923-4

[11] B. Wu, K. Li, L. Wang, K. Yin, M. Nie et al., Revolutionizing Sensing Technologies: A Comprehensive Review of Flexible Acceleration Sensors. FlexMat **2**(1), 55 (2025). https://doi.org/10.1002/flm2.38

[12] C. Wu, X. Gao, H. Zhu, X. Wang, S. Wang et al., Multiscale Stress Transmission Regulation toward Flexible Strain Sensors with High Stability. Adv. Funct. Mater. **36**(5), e10852 (2025). https://doi.org/10.1002/adfm.202510852

[13] Y. Xiong, Y. Liu, J. Yang, M. Chen, Z. L. Wang et al., Bioinspired Triboelectric-Driven Multisensory Framework with Autonomous Cross-Modal Adaptation. eScience **6**(2), 100482 (2026). https://doi.org/10.1016/j.esci.2025.100482

[14] Q. Mao, Z. Liao, J. Yuan, and R. Zhu, Multimodal Tactile Sensing Fused with Vision for Dexterous Robotic Housekeeping. Nat. Commun. **15**(1), 6871 (2024). https://doi.org/10.1038/s41467-024-51261-5

[15] T. Wang, T. Jin, W. Lin, Y. Lin, H. Liu et al., Multimodal Sensors Enabled Autonomous Soft Robotic System with Self-Adaptive Manipulation. ACS Nano **18**(14), 9980 (2024). https://doi.org/10.1021/acsnano.3c11281

[16] J. Li, Z. Xu, N. Li, K. Zhang, G. Xiong et al., Ai-Embodied Multi-Modal Flexible Electronic Robots with Programmable Sensing, Actuating and Self-Learning. Nat. Commun. **16**(1), 8818 (2025). https://doi.org/10.1038/s41467-025-63881-6

[17] X. An, S. Niu, J. Chen, X. Zhang, J. Zhang et al., Flexible Electronics in Robotics Systems: From Devices to Applications. SmartBot **2**(1), e70017 (2026). https://doi.org/https://doi.org/10.1002/smb2.70017

[18] J. Yu, S. Xian, Z. Zhang, X. Hou, J. He et al., Synergistic Piezoelectricity Enhanced Batio3/Polyacrylonitrile Elastomer-Based Highly Sensitive Pressure Sensor for Intelligent Sensing and Posture Recognition Applications. Nano Res. **16**(4), 5490 (2022). https://doi.org/10.1007/s12274-022-5084-x

[19] H. Zhao, W. Qian, C. Guo, Y. Zhang, J. Wang et al., A Switchable Dynamic-Static Tactile System for Augmented Haptic Secret Communication. Sci. Adv. **11**(37), eadx6959 (2025). https://doi.org/doi:10.1126/sciadv.adx6959

[20] J. Zhou, H. Chen, Z. Wu, P. Zhou, M. You et al., 2d Ti3c2tx Mxene-Based Light-Driven Actuator with Integrated Structure for Self-Powered Multi-Modal Intelligent Perception Assisted by Neural Network. Nano Energy **134**, 110552 (2025). https://doi.org/10.1016/j.nanoen.2024.110552

[21] J. Zhang, Y. Hu, L. Zhang, J. Zhou, and A. Lu, Transparent, Ultra-Stretching, Tough, Adhesive Carboxyethyl Chitin/Polyacrylamide Hydrogel toward High-Performance Soft Electronics. Nano-Micro Lett. **15**(1), 8 (2022). https://doi.org/10.1007/s40820-022-00980-9

[22] Y. Jiang, Z. Huang, H. Xie, L. Yang, F. Kang et al., Wide-Range Stretchable Modulus Sensor Based on Psss Architecture for Tactile Perception. Adv. Funct. Mater. **36**(36), e30485 (2026). https://doi.org/10.1002/adfm.202530485

[23] J. Ji, H. Luo, J. Su, S. Wang, X. Chen et al., Multisensory Electronic Skin with Decoupled Pressure-Temperature-Sensing Capabilities for Similar Object Recognition. PNAS **122**(41), e2519693122 (2025). https://doi.org/10.1073/pnas.2519693122

[24] Y. Qiu, Z. Wang, P. Zhu, B. Su, C. Wei et al., A Multisensory-Feedback Tactile Glove with Dense Coverage of Sensing Arrays for Object Recognition. Chem. Eng. J. **455**, 140890 (2023). https://doi.org/10.1016/j.cej.2022.140890

[25] S. Li, T. Wu, J. Xu, Y. Huang, Z. Zhang et al., Biomimetic Multimodal Tactile Sensing Enables Human-Like Robotic Perception. Nature Sensors **1**(1), 52 (2026). https://doi.org/10.1038/s44460-025-00006-y

[26] C. Chen, Z. Liu, L. Guo, B. Huo, Q. Sun et al., High Spatiotemporal Resolution Biomimetic Thermoreceptors Realizing by Jointless P-N Integration Thermoelectric Composites. Adv. Funct. Mater. **34**(49), 2411490 (2024). https://doi.org/10.1002/adfm.202411490

[27] X. Xu, F.-L. Gao, L. Tian, Z.-Y. Yang, Z.-Z. Yu et al., Ultra-Sensitive and High-Resolution Flexible Thermoelectric Sensor Enabled by P-N Heterojunction Array Structure. Matter **8**(11), 102265 (2025). https://doi.org/10.1016/j.matt.2025.102265

[28] J. Zhang, X. Cong, X. Yu, Y. Luo, and Y. Hu, A Dual-Function Piezoelectric Device for Integrated Energy Harvesting and Stiffness Sensing. IEEE Sens. J. **25**(19), 37132 (2025). https://doi.org/10.1109/jsen.2025.3593956

[29] H. Bassal, Y. Abbass, C. Gianoglio, and M. Valle, Hardness Discrimination Using Piezoelectric-Based Biomimetic Tactile Sensor and Machine Learning. IEEE Sensors Letters **8**(8), 1 (2024). https://doi.org/10.1109/lsens.2024.3431430

[30] J. Yao, X. Yu, W. Gao, F. He, X. Chen et al., A Multi-Functional Flexible Tactile Sensing Device for Material Identification. MEASUREMENT **257**, 118623 (2026). https://doi.org/10.1016/j.measurement.2025.118623

[31] K. Kong, L. Wang, H. Wu, Z. Le, Y. Zhang et al., Skin-Inspired Multimodal Tactile Sensor Aiming at Smart Space Extravehicular Multi-Finger Operations. Chem. Eng. J. **498**, 154870 (2024). https://doi.org/10.1016/j.cej.2024.154870

[32] Q. Wang, B. Yan, M. Wang, H. Yu, H. Zhang et al., The Tactile Force Sensing of the Gripper Based on the Mode Interference Fiber Sensor. IEEE Sens. J. **24**(19), 29716 (2024). https://doi.org/10.1109/jsen.2024.3438851

[33] V. Del Bono, E. Capaldi, A. Kelshiker, A. Aktas, H. Aihara et al., Multi-Modal Sensing in Colonoscopy: A Data-Driven Approach. IEEE Rob. Autom. Lett. **11**(2), 2018 (2026). https://doi.org/10.1109/lra.2025.3645700

[34] X. Guo, Z. Sun, Y. Zhu, and C. Lee, Zero-Biased Bionic Fingertip E-Skin with Multimodal Tactile Perception and Artificial Intelligence for Augmented Touch Awareness. Adv. Mater. **36**(39), e2406778 (2024). https://doi.org/10.1002/adma.202406778

[35] C. Han, Z. Cao, Z. An, Z. Zhang, Z. L. Wang et al., Multimodal Finger-Shaped Tactile Sensor for Multi-Directional Force and Material Identification. Adv. Mater. **37**(19), e2414096 (2025). https://doi.org/10.1002/adma.202414096

[36] V. Gautham, A. Panpalia, H. Manouchehri, K. K. Gabani, V. Anil et al., Slip-Actuated Bionic Tactile Sensing System with Dynamic Dc Generator Integrated E-Textile for Dexterous Robotic Manipulation. Nat. Commun. **16**(1), 7005 (2025). https://doi.org/10.1038/s41467-025-61843-6

[37] C. Han, J. Lv, C. Dong, J. Li, Y. Luo et al., Classification, Advanced Technologies, and Typical Applications of End-Effector for Fruit and Vegetable Picking Robots. Agriculture **14**(8), 1310 (2024). https://doi.org/10.3390/agriculture14081310

[38] T. Noreen, A. Ali, S. Anwar, S. Farooq, W. A. Altabey et al., Implementation of Fruit Plucking Robot in Apple Harvesting: A Review. Results in Engineering **27**, (2025). https://doi.org/10.1016/j.rineng.2025.106575

[39] M. Ji, Z. Wang, J. Wu, L. Huang, M. Zheng et al., Machine Learning–Assisted Triboelectric Nanogenerator Technology for Intelligent Sports. Sci. Adv. **11**(40), eadz3515 (2025). https://doi.org/doi:10.1126/sciadv.adz3515

[40] W. Peng, R. Zhu, Q. Ni, J. Zhao, X. Zhu et al., Functional Tactile Sensor Based on Arrayed Triboelectric Nanogenerators. Adv. Energy Mater. **14**(44), 2403289 (2024). https://doi.org/10.1002/aenm.202403289

[41] P. Lu, X. Liao, X. Guo, C. Cai, Y. Liu et al., Gel-Based Triboelectric Nanogenerators for Flexible Sensing: Principles, Properties, and Applications. Nano-Micro Lett. **16**(1), 206 (2024). https://doi.org/10.1007/s40820-024-01432-2

[42] W. Kwak, J. Yin, S. Wang, and J. Chen, Advances in Triboelectric Nanogenerators for Self-Powered Wearable Respiratory Monitoring. FlexMat **1**(1), 5 (2024). https://doi.org/10.1002/flm2.10

[43] X. Ma, E. Kim, J. Zhou, J. Gao, C. Kim et al., Self-Powered Smart Skins for Multimodal Tactile Perception Based on Triboelectric and Hygroelectric Working Principles. Nano Energy **113**, 108589 (2023). https://doi.org/10.1016/j.nanoen.2023.108589

[44] G. Du, J. Zhao, Y. Shao, T. Liu, B. Luo et al., A Self-Damping Triboelectric Tactile Patch for Self-Powered Wearable Electronics. eScience **5**(2), 100324 (2025). https://doi.org/10.1016/j.esci.2024.100324

[45] L. Gao, K. Liu, W. Wang, X. Li, Q. Deng et al., Intelligent Soft Robotic System for Sensing and Recognition Via Triboelectric-Based Multi-Sensor Fusion. Adv. Funct. Mater. **36**(8), e17158 (2025). https://doi.org/10.1002/adfm.202517158

[46] J. Huang, S. G. S. Ka, H. Cheong, Y. Zhang, D. Chu et al., Tactile Augmentation of Material Classification Via Imperceptible on-Skin Triboelectricity Collection. Adv. Sci. **12**(31), e00217 (2025). https://doi.org/10.1002/advs.202500217

[47] T. S. Bincy, A. P. S. Prasanna, M. Anithkumar, and S.-J. Kim, Enhanced Tactile Perception for Human–Machine Interaction Using a Triboelectric Touchpad. ACS Appl. Electron. Mater. **7**(7), 2955 (2025). https://doi.org/10.1021/acsaelm.5c00147

[48] J. Yuan, J. He, J. Yu, S. Shi, Y. Chang et al., An Enhanced Flexible Triboelectric Tactile Sensor for Material Classification and Roughness Recognition. SCI CHINA TECHNOL SC **68**(4), 1420205 (2025). https://doi.org/10.1007/s11431-024-2891-y

[49] S. He, Y. Zhou, S. Sun, Z. Long, F. Chen et al., Sub-Milliscale-Resolution Bimodal Tactile Sensor Array with Human-Skin-Like Graphesthesia Sensation. Adv. Mater. **38**(13), e19734 (2026). https://doi.org/10.1002/adma.202519734

[50] Y. Long, B. Jiang, T. Huang, Y. Liu, J. Niu et al., Super-Stretchable, Anti-Freezing, Anti-Drying Organogel Ionic Conductor for Multi-Mode Flexible Electronics. Adv. Funct. Mater. **33**(41), 2304625 (2023). https://doi.org/10.1002/adfm.202304625

[51] Y. Zhou, X. Zhao, J. Xu, Y. Fang, G. Chen et al., Giant Magnetoelastic Effect in Soft Systems for Bioelectronics. Nat. Mater. **20**(12), 1670 (2021). https://doi.org/10.1038/s41563-021-01093-1

[52] G. Tian, L. Guo, Y. Gao, W. Deng, S. Wang et al., A Wearable All-in-One Obstructive Sleep Apnea Management System with Flexible Piezoelectric Monitoring and Soft Magnetoelastic Stimulating. Matter **8**(11), 102323 (2025). https://doi.org/10.1016/j.matt.2025.102323

[53] Y. H. Zhou, G. R. Chen, X. Zhao, T. Tat, Z. Q. Duan et al., Theory of Giant Magnetoelastic Effect in Soft Systems. Sci. Adv. **11**(1), 14 (2025). https://doi.org/10.1126/sciadv.ads0071

[54] H. Hou, Z. Xiang, C. Zhi, H. Hu, X. Zhu et al., Optimized Magnetization Distribution in Body-Centered Cubic Lattice-Structured Magnetoelastomer for High-Performance 3d Force-Tactile Sensors. SENSORS-BASEL **25**(7), 2312 (2025). https://doi.org/10.3390/s25072312

[55] Y. Zhou, X. Zhao, J. Xu, G. Chen, T. Tat et al., A Multimodal Magnetoelastic Artificial Skin for Underwater Haptic Sensing. Sci. Adv. **10**(1), eadj8567 (2024). https://doi.org/doi:10.1126/sciadv.adj8567

[56] Y. Liu, Y. Chen, Z. Liu, H. Qin, and J. Guo, A Bioinspired 3d Tactile Force Sensor under Deep-Sea High Hydrostatic Pressure Environments for Underwater Robotic Adaptive Grasping. ACS Appl. Mater. Interfaces **18**(1), 2662 (2026). https://doi.org/10.1021/acsami.5c20573

[57] T. Jin, Z. Sun, L. Li, Q. Zhang, M. Zhu et al., Triboelectric Nanogenerator Sensors for Soft Robotics Aiming at Digital Twin Applications. Nat. Commun. **11**(1), 5381 (2020). https://doi.org/10.1038/s41467-020-19059-3

[58] Y. Zhang, N. Li, L. Zhang, J. Lin, X. Gao et al., A Review on the Recent Developments in Vision-Based Apple-Harvesting Robots for Recognizing Fruit and Picking Pose. Comput. Electron. Agric. **231**, 109968 (2025). https://doi.org/10.1016/j.compag.2025.109968

[59] M. Hobart, M. Pflanz, N. Tsoulias, C. Weltzien, M. Kopetzky et al., Fruit Detection and Yield Mass Estimation from a Uav Based Rgb Dense Cloud for an Apple Orchard. Drones **9**(1), 60 (2025). https://doi.org/10.3390/drones9010060

[60] Q. Zheng, X. Dai, Y. Wu, Q. Liang, Y. Wu et al., Self-Powered High-Resolution Smart Insole System for Plantar Pressure Mapping. BMEMat **1**(1), (2023). https://doi.org/10.1002/bmm2.12008

[61] X. Lu, T. Wang, S. Zhong, T. Cao, C. Zhou et al., Self-Powered Multimodal Tactile Sensing Enabled by Hybrid Triboelectric and Magnetoelastic Mechanisms. Cyborg and Bionic Systems **6**, 0320 (2025). https://doi.org/10.34133/cbsystems.0320

[62] W. Liu, Y. Duo, X. Chen, B. Chen, T. Bu et al., An Intelligent Robotic System Capable of Sensing and Describing Objects Based on Bimodal, Self-Powered Flexible Sensors. Adv. Funct. Mater. **33**(41), 2306368 (2023). https://doi.org/10.1002/adfm.202306368

[63] Y. Jin, S. a. Xue, and Y. He, Flexible Pressure Sensors Enhanced by 3d-Printed Microstructures. Adv. Mater. **37**(27), 2500076 (2025). https://doi.org/10.1002/adma.202500076

[64] N. Li, H. Li, J. Feng, Y. Jiu, H. Niu et al., Microstructure-Modulated Linear-Response Flexible Pressure Sensors. Adv. Funct. Mater. **36**(2), e09776 (2025). https://doi.org/10.1002/adfm.202509776

[65] S. C. Mannsfeld, B. C. Tee, R. M. Stoltenberg, C. V. Chen, S. Barman et al., Highly Sensitive Flexible Pressure Sensors with Microstructured Rubber Dielectric Layers. Nat. Mater. **9**(10), 859 (2010). https://doi.org/10.1038/nmat2834

[66] F. Ejehi, R. Mohammadpour, E. Asadian, S. Fardindoost, and P. Sasanpour, Enhancement of Self-Powered Humidity Sensing of Graphene Oxide-Based Triboelectric Nanogenerators by Addition of Graphene Oxide Nanoribbons. Microchim. Acta **188**(8), 251 (2021). https://doi.org/10.1007/s00604-021-04921-y

[67] V. Mohan, V. K. Mariappan, P. Pazhamalai, K. Krishnamoorthy, and S.-J. Kim, Unravelling the Impact of Carbon Allotropes in Flexible Polydimethylsiloxane Film Towards Self-Powered Triboelectric Humidity Sensor. CARBON **205**, 328 (2023). https://doi.org/10.1016/j.carbon.2023.01.022

[68] Y. Lee, M. Lee, J. Lee, H. W. Jang, and J. S. Jang, Hydrovoltaic Power Generation Depend on Wettability at the Liquid-Solid Interface: Mechanisms, Materials, and Applications with Various Resource. Exploration **5**(2), 70007 (2025). https://doi.org/10.1002/EXP.70007

Publisher's Note

Springer Nature remains neutral with regard to jurisdictional claims in published maps and institutional affiliations.